Article

3D hydrogel platform with macromolecular actuators for precisely controlled mechanical forces on cancer cell migration

Bohan Li[1,2,3], Qingyu Fu[1,2,3], Yan Lu[1,2], Cheng Chen[1,2], Yingshuai Zhao[1,2], Yuanfeng Zhao[1,2], Minghui Cao[1,2], Wei Zhou[1,2], Xiaoliang Fan[1,2], Xiaoyu Jiang[1,2], Peng Zhao[1,2] & Yijun Zheng [1,2] ✉

Mechanical forces play a critical role in regulating cancer cell behavior, particularly during metastasis. Here we present a three-dimensional hydrogel platform embedded with near-infrared-responsive macromolecular actuators that enable precise mechanical stimulation of specific integrin subtypes in cancer cells. By leveraging this system, we investigate how different force parameters—magnitude, frequency, and duration—affect the migration and invasion of ovarian cancer cell spheroids, focusing on the integrins αvβ3 and αvβ6. We find that mechanical stimulation enhances collective invasion at early stages and triggers a mesenchymal-to-amoeboid transition during later migration, especially when high-frequency, large-amplitude forces disrupt αvβ3-ligand interactions. In contrast, cells engaging αvβ6—through higher-affinity binding—show limited transition under similar conditions. Molecular simulations support these findings by revealing the underlying mechanics of integrin-specific responses. This 3D hydrogel platform provides a powerful tool for studying mechanotransduction in cancer cells and offers potential insights for developing targeted cancer therapies.

The intricate relationship between active physical forces and cellular behavior is pivotal to a variety of physiological processes, including embryonic development[1], wound healing[2], and the pathogenesis of diseases such as cancer[3]. In cancer, metastasis is a complex and multifaceted process that significantly contributes to cancer mortality, with the ability of cancer cells to switch between different migration modes playing a crucial role[4]. Physical cues from the extracellular matrix influence mechanosignaling pathways and cytoskeletal architecture, thereby determining the migratory behavior of cancer cells, which impacts their invasiveness, dissemination, and overall metastatic potential[5,6]. Understanding these nuances is crucial for developing targeted therapies that can effectively alter malignant cell migration and metastasis[7].

Advanced material platforms offer a promising avenue for systematically investigating how active mechanical forces influence cancer cell metastasis[8]. Various methods exist to apply mechanical stimulation to cells, including mechanical stretching devices[9], elastic substrates[10], compression devices[11], electrical stimulation[12], and magnetic stimulation[13]. The variability inherent in active mechanical stimulation such as force amplitude[14], frequency[15], duration[16], loading rate[17] and spatial distribution[18] adds layers of complexity to understanding its effects on cellular behaviors. One major limitation of traditional force application methods is their tendency to deliver non-specific mechanical stimulation, leading to significantly different outcomes. For instance, Riveline et al. showed that applied mechanical force using a micropipette can lead to focal adhesion assembly and elongation, thereby mediating integrin-dependent cell migration[19]. Conversely, Piotrowski-Daspit et al. found that when subject to shear flow, cancer cells exhibit reduced adhesion and increased integrin-independent amoeboid-like migration, suggesting

[1]School of Physical Science and Technology, ShanghaiTech University, Shanghai, China. [2]State Key Laboratory of Advanced Medical Materials and Devices, ShanghaiTech University, Shanghai, China. [3]These authors contributed equally: Bohan Li, Qingyu Fu. ✉e-mail: zhengyj@shanghaitech.edu.cn

that certain mechanical forces can lead to amoeboid transitions[20]. The reason for that is the mechanical force required to signal is receptor-specific. These methods struggle to achieve precise mechanical loading at a microscopic level and to target specific receptor proteins at the nanoscale during the force application process, making comprehensive study of the molecular mechanisms of cellular mechanotransduction challenging.

Integrins, located on the cell membrane, are among the most important mechanosensors, playing a crucial role in how cells interpret and respond to mechanical stimuli[21]. For instance, integrin subtypes such as integrin αvβ6 and RGD-binding integrins like αvβ3 play distinct roles in cell-matrix adhesion and mechanotransduction[22,23]. Specifically, integrin αvβ6 requires a higher tension of approximately 200 pN to activate cell spreading[24], a requirement that starkly contrasts with the lower, cell type-independent threshold of around 40 pN needed for RGD-binding integrins[25]. These findings underscore the differences in mechanical force requirements and responses among integrin subtypes. Given this complexity, there is a pressing need to develop a material platform capable of precise force application to specific receptors on the cell membrane. Such a platform would allow for targeted mechanical stimulation, enabling a more detailed and accurate investigation of the mechanotransduction pathways mediated by various receptor subtypes and their roles in cellular processes and disease states.

Molecular force application tools enable precise mechanical loading on targeted receptors. By leveraging chemical methods to accurately integrate into interface materials for cell stimulation, these tools are increasingly becoming an effective pathway for constructing platforms for primary mechanical stimulation. Examples include light-driven molecular motor rotation[26], light-induced azobenzene conformational changes[15] and the phase transition of cross-linked thermo-responsive polymer nanoparticles[27]. Existing force application molecules were utilized only on 2D surfaces, leading to unnatural physiological responses compared to the significantly different effects observed in 3D in vivo environments[28]. Therefore, it is of

immense interest to gain a comprehensive understanding of how cancer cells respond to active mechanical stimulation in a more physiologically relevant 3D context.

Herein, we develop molecular actuators CD-PNIPAM-Ligand featuring a croconaine dye (CD) chromophore with strong absorption near 800 nm. Upon NIR light illumination, the CD groups convert light to heat, causing the thermal responsive PNIPAM chains to shrink and apply a tensile force directly onto the cellular receptor[29]. We incorporate these actuators into a spheroid-embedded Dextran-based hydrogel to apply forces to specific cellular receptors in a 3D microenvironment (Fig. 1). Leveraging this hydrogel platform, we investigate the impact of force stimulation parameters, including magnitude, frequency and duration on cell migration and invasion of ovarian cancer Hey cell spheroids. To specifically compare the effects of force application on different integrin subtypes, we functionalize the actuators with two subtype-specific peptidomimetic ligands: RGD for αvβ3 and RTDLDSLRT (referred to as RTD) for αvβ6, respectively. Our findings demonstrate that force application can enhance collective cell invasion in the early stages. In later stages, we observe a pronounced mesenchymal-to-amoeboid transition (MAT) induced by disrupting the RGD-αvβ3 complex under higher force application frequency and amplitude. In contrast, this transition is almost absent in cells stimulated through the RTD-αvβ6 complex. We use molecular mechanics simulation to validate the different pathway impacts and highlight the importance of mechanical force parameters and their specific interaction with integrin subtypes in modulating cell migration.

Results
Developing hydrogels with molecular actuators for three-dimensional cell culture
When selecting a hydrogel cross-linking approach for three-dimensional cell cultures, it's crucial to consider factors such as cross-linking chemistry, gelation time, polymer network structure, and buffer conditions. The most widely adopted strategy for 3D cell culture
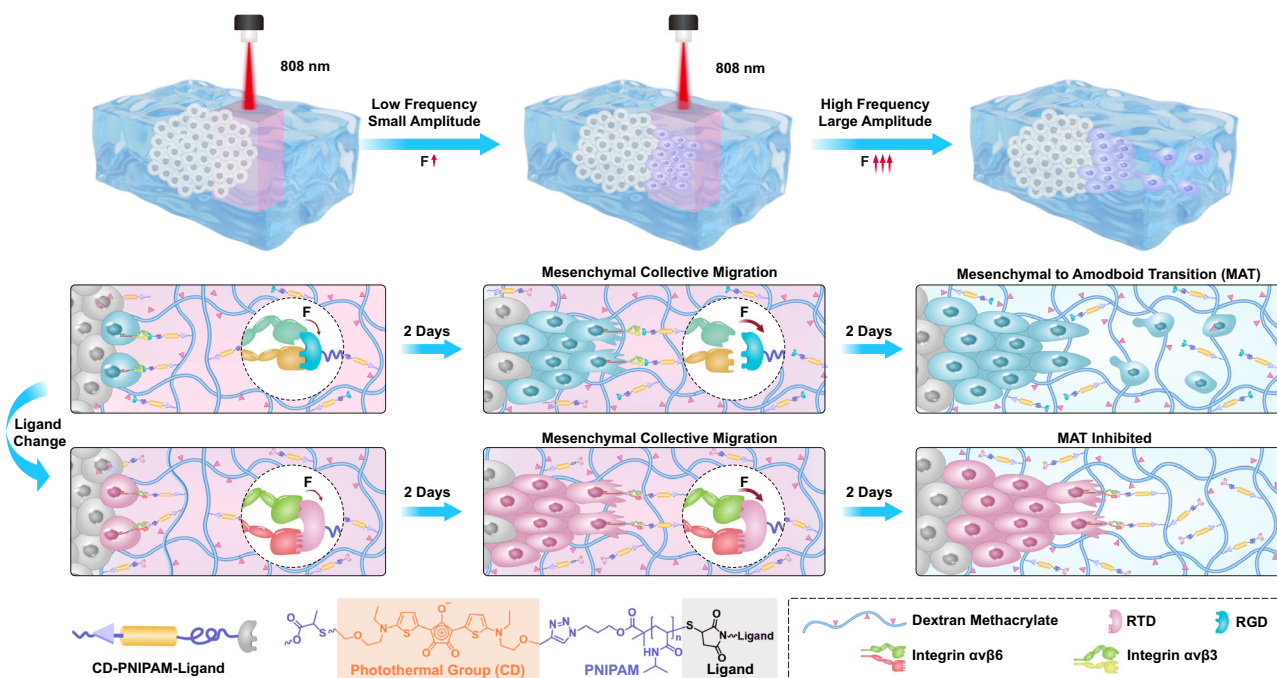

Fig. 1 | The design and operational mechanism of the hydrogel platform. Schematic of cell migration manipulation using a 3D DexMA hydrogel platform functionalized with molecular actuators CD-PNIPAM-Ligand, modulated by NIR light. The cell spheroid is encapsulated within the hydrogel. When functionalized with two different subtype-specific peptidomimetic ligands— RGD for αvβ3 and RTDLDSLRT (referred to as RTD) for αvβ6—distinct cell migration patterns were observed after 4 days under various force application parameters.
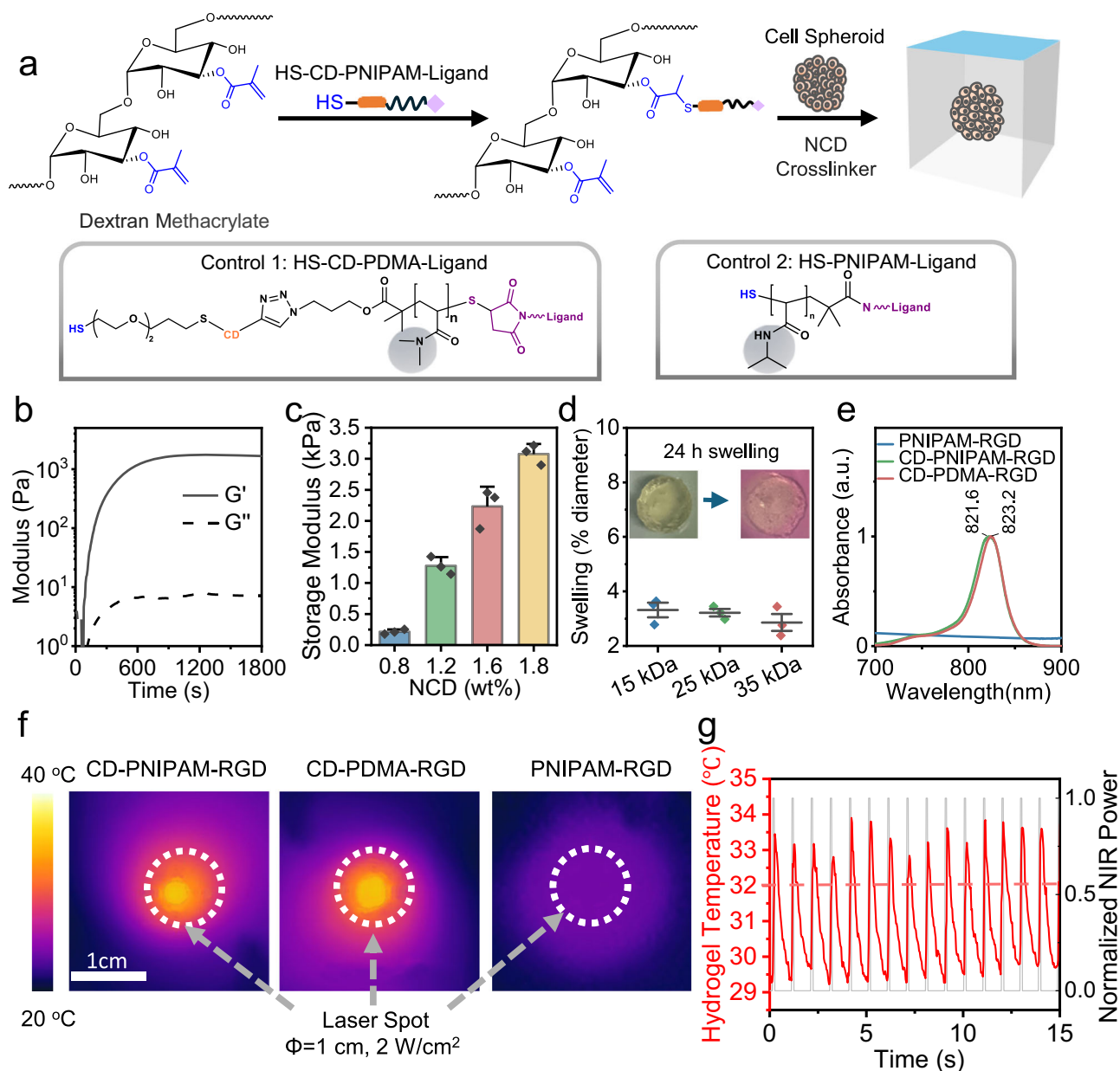
Fig. 2 | Preparation, mechanical and photothermal properties of DexMA hydrogels functionalized with macromolecular actuators. a Schematic depiction of the preparation of DexMA hydrogels and cell encapsulation process. **b** Time-dependent storage modulus (G′) and loss modulus (G″) of DexMA hydrogels. **c** Variation of storage modulus (G′) in DexMA hydrogels with different concentrations of the crosslinker (NCD peptide). The study included three replicates for each group (*n* = 3). **d** Swelling behaviors of hydrogels composed of DexMA with grafted CD-PNIPAM-RGD of varying molecular weights. The study included three replicates for each group (*n* = 3). **e** UV–vis–NIR absorption spectra of DexMA hydrogels functionalized with CD-PNIPAM-RGD, CD-PDMA-RGD and PNIPAM-RGD. **f** Representative thermal images obtained during photothermal heating of DexMA hydrogels functionalized with CD-PNIPAM-RGD, CD-PDMA-RGD and PNIPAM-RGD under 808 nm laser irradiation (6.6 μW/μm²), scale bar = 1 cm. **g** The temperature fluctuations of the DexMA hydrogel area functionalized with CD-PNIPAM-TTC under 808 nm laser exposure (6.6 μW/μm², 1 Hz, 10% duty cycle; ground temperature = 29 °C), captured by an IR camera. The data in (**b**, **c**) are presented as mean values ± S.D.

is Michael-type addition reactions[30], favored for their suitable gelation kinetics and the high viability of encapsulated cells. In this work, we prepared hydrogels based on Dextran (70 kDa), which has been functionalized with methacrylate groups at a 71% degree of functionalization, referred to as Dextran-MA. The pre-prepared molecular actuator HS-CD-PNIPAM-RGD was synthesized through asymmetric reactions (detailed in the supporting information) for targeting to α5β1 and αvβ3 integrins. One end was initially modified with a complementary ligand, 3-maleimidopropionyl RGD, via thiol-ene addition. The other end of the actuator was then converted into thiols to facilitate incorporation into hydrogel chains. It has been reported that RGD concentrations ranging between 25 μM and 3.5 mM support 3D cell adhesion and

spreading in 3D hydrogels[5,31]. We utilized a total RGD concentration of 1 mM to optimize adhesion sites while maintaining the cross-linking capability in DexMA macromers. Finally, the actuator-functionalized DexMA macromers were crosslinked through Michael-type addition using a matrix metalloproteinase (MMP) sensitive dicysteine peptide (CGPQGIAGQGCR, referred to NCD crosslinker) in the presence of spheroids, as illustrated in Fig. 2a. Thermo-inert poly(N, N-dimethyla-crylamide) (HS-CD-PDMA-RGD) and CD-free HS-PNIPAM-RGD were also synthesized and incorporated into hydrogels as controls (see supporting information for synthetic details). Sulfhydryl group of HS-CD-PNIPAM-RGD is reactive at pH=8, enabling the thiol-ene click reaction to complete within 30 minutes.

The fast gelation times are critically important for uniform distribution of encapsulated spheroids in 3D cultures. Rheological measurements revealed that our hydrogel achieved a plateau of 1.2 kPa in shear storage modulus (G′) within 15 min under near-physiological conditions (Fig. 2b). pH-Tunability, a characteristic of nucleophilic thiol-based crosslinking reactions, enables the adjustment of gelation times within a pH range of 7–9 (Supplementary Fig. 1a, b). This flexibility allows for gelation to occur on a timescale that facilitates sufficient mixing, leading to uniform network structures and evenly distributed spheroids.

The ultimate G′ of the hydrogels was found to be tunable. We maintained the concentration of DexMA at 8 wt% while varying the concentration of the NCD crosslinker. By adjusting the crosslinker concentration in the final mixture from 10 to 30 mM, corresponding to 1.2 to 2.0 wt%, we observed a range in storage modulus from 200 to 3000 Pa (Fig. 2c). This variation demonstrates that the mechanical properties of our hydrogel platform can be finely tuned to accommodate diverse cell culturing conditions. The swelling ratio of a hydrogel is a key indicator of its overall network structure. A high level of methacrylate functionalization at 75% reduces the hydrogel's swelling capacity[32]. This was confirmed by measuring the hydrogel's diameter before and after immersion in RPMI 1640 culture medium for 24 h, where we detected no significant differences in groups with identical chemical grafting concentrations of CD-PNIPAM-RGD with different molecular weights (Fig. 2d). Additionally, the storage modulus remained unchanged with extended immersion time, further confirming the hydrogel's structural stability (Supplementary Fig. 1c). Such non-swelling behavior ensures a consistent and robust scaffold conductive to cell attachment and growth. The resultant stability of the hydrogel is pivotal for preserving the 3D cell culture's structural integrity, facilitating experiments that are both more reliable and reproducible over time.

The integration of the CD-PNIPAM-RGD/CD-PDMA-RGD actuator into the dextran-MA gel was confirmed using UV-spectroscopy. Thin films of the hydrogel, supported on quartz substrates, exhibited an absorption peak at 793.8 nm. This peak aligns with the λ_{max} characteristic of the CD group. Conversely, hydrogels incorporated with PNIPAM-RGD lacking the CD photothermal group did not demonstrate any infrared absorption, underscoring the specific contribution of the CD component to the gel's absorbance profile (Fig. 2e). Further investigation into the hydrogels' photothermal effects was conducted using a commercial thermal camera to monitor the apparent temperature (A.T.). Subjecting the hydrogel to an 808 nm laser at a power density of 2 W/cm² led to an increase in A.T. at the irradiated spots of hydrogel substrates containing CD-PNIPAM-TTCs and CD-PDMA-TTCs, unlike those with PNIPAM-TTCs. This observation underscores the CD group's role in facilitating an efficient photothermal effect (Fig. 2f). Additionally, when subjected to pulsed near-infrared (NIR) light (6.6 μW/μm², 1 Hz, and a 10% duty cycle), the hydrogels demonstrated quick temperature changes from 29 °C to 32 °C within milliseconds, as shown in Fig. 2g. Thus, we concluded that, upon the operating temperature set lower than 32 °C, NIR pulsed illumination could induce thermoresponsive expanded/globule conformation changes in CD-PNIPAM-TTCs. Notably, the polymer collapse upon exceeding the LCST occurs on a microsecond timescale[33]. Consequently, the force generated by our molecular force actuator during one actuation cycle resembles a rapid pulse, dictated primarily by the local temperature dynamics rather than a prolonged step change. Furthermore, photothermal studies conducted across a range of power densities (0.52 to 16.4 μW/μm²) revealed localized temperature rise of 2–9 °C, which was sufficient to trigger PNIPAM's conformational transition while compromising cell viability (see Supplementary Fig. 2).

To investigate the capacity of these hydrogels to facilitate cell activity, Hey cell spheroids were embedded within 8% (wt/v) Dextran-

MA hydrogels (50 μL) and cultured over a period of three days, after which they were subjected to Live/Dead staining (Invitrogen) (see Supplementary Fig. 3). Hey cells encapsulated in hydrogels lacking HS-CD-PNIPAM-RGD functionalization remained localized to their initial spheroid, showing no migration into the surrounding hydrogel matrix (Supplementary Fig. 4). Conversely, hydrogels modified with HS-CD-PNIPAM-RGD supported the Hey cell' migration away from the original spheroid, demonstrating the successful integration of the RGD moiety and its effect in promoting cellular migration (refer to Fig. 2a).

Mechanical stimulation enhances collective-cell invasion

We first used this model to investigate how the initial collective-cell invasion is regulated by mechanical stimulation by targeting integrin subtype α5β1 and αvβ3. Hey cells exhibited collective movement, with motile cells at the leading invasive edge generating adhesion and traction forces through the mesenchymal mode. In this mode, the leading cells formed adhesions to the extracellular matrix (ECM), specifically through RGD-integrin complexes in our context. Circular areas (15,000 μm²) of the spheroids were exposed to illumination after being seeded into hydrogel for one day.

Analysis of the maximal migration distances within these illuminated zones (ROI1, depicted in Fig. 3a, d) revealed that cells in hydrogels modified with CD-PNIPAM-RGD migrated an average distance of approximately 84 μm away from the spheroid after 2 days. In contrast, in areas not subjected to illumination (ROI2, shown in Fig. 3a), the migration distance was measured at 52 μm. To eliminate potential effects from cellular protrusions adapting to NIR irradiation, comparable experiments were conducted with spheroids in control hydrogels linked to PNIPAM-RGD and CD-PDMA-RGD (Fig. 3b, c). In these instances, cell migration distances remained unchanged regardless of NIR illumination (Fig. 3e, f). These findings corroborate that photothermal-induced contraction of macromolecular actuators can generate pulling forces, significantly facilitating Hey cell mesenchymal collective migration in 3D (Fig. 3a, d). We propose that the applied force enhances focal adhesion complexes, which in turn activate actin cytoskeleton signaling pathways, thereby facilitating mesenchymal motility. We performed F-actin staining on the cells to analyze the arrangements of F-actin. Our observations revealed that F-actin exhibited different configurations in the illuminated versus non-illuminated regions. Specifically, actin anisotropy measurements were 10% in the non-illuminated ROI2 and 25% in the illuminated ROI1 (Supplementary Fig. 5c). The average F-actin filament fluorescent strength 67% in ROI1 higher than in ROI2 (Supplementary Fig. 5d). This discrepancy underscores the significant influence of applied force on altering the architecture of the cellular skeleton. Furthermore, we investigated the formation of focal adhesions (FAs) in the illuminated region (ROI1) as compared to the non-illuminated area of the spheroid. Typically, FAs are key adhesion structures that facilitate various cell-signaling pathways but are seldom observed in cells cultured in non-fibrillar 3D hydrogels[34]. Our examination focused on vinculin and αvβ3-integrin. In the illuminated region, we observed intense and punctate clusters of αvβ3-integrin at the spouting Hey cells (Fig. 3g). These integrin clusters were associated with strong vinculin localization, indicating FA formation. Additionally, αvβ3-integrin: vinculin complexes were found to couple with the actin cytoskeleton at the protrusive tips, providing further evidence of FA formation. In non-illuminated regions, β1-integrin and vinculin staining appeared diffused along the cell periphery. The colocalization of αvβ3-integrin and vinculin was significantly reduced compared to the illuminated regions, even at the few protrusive sites that were observed. We also examined β1-integrin and paxillin, which also show clustering after illumination (Supplementary Fig. 6). Quantification of the percentage of cells with FAs across three replicates revealed a significantly higher frequency of FA formation in cells subjected to force stimulation.

Notably, there was a significant difference in the percentage of cells with FA between the stimulated and control groups, suggesting enhanced cell-ECM adhesions in response to applied force (Fig. 3h).

We expanded our exploration into force-enhanced cellular migration under varied conditions. To assess the impact of actuation frequency on cell migration, three pulsing conditions were tested, including frequencies of 0.1, 1, and 10 Hz (Fig. 4a). These conditions

resulted in average migration displacements ranging from 84 to 137 µm (Fig. 4b), suggesting that a higher actuation frequency enhances mechanical stimulation efficiency (Supplementary Fig. 7) Additionally, increasing the NIR exposure power density from 0.52 to 16.4 µW/µm^2 led to an increase in the displacement of actin patches from 85 to 143 µm (Fig. 4c). This implies that higher laser powers, expected to induce a higher microthermal temperature, result in a more

Fig. 3 | Impact of force stimulation on cell migration in DexMA 3D hydrogels. **a**–**c** Representative brightfield and fluorescence images of cells in a DexMA 3D hydrogel grafted with CD-PNIPAM-RGD. (**a**), CD-PDMA-RGD (**b**), PNIPAM-RGD (**c**) each with a molecular weight of 15 kDa under 9.2 μW/μm², 10 Hz NIR illumination Cells were tracked over time during NIR illumination. The illuminated area is demarcated by a dashed red circle. Scale bars = 50 μm. Incubation temperature = 25 °C. Actin and nuclei are visualized as green and blue, respectively. **d** Graph depicting the mean relative increase in sprout length of spheroids encapsulated in hydrogels conjugated with CD-PNIPAM-RGD over time, within two defined regions of interest: ROI1(NIR illuminated) and ROI2 (non-illuminated). n = 55, 47 cells respectively. ***P < 0.001 **e**–**f** Identical experiments conducted with control

hydrogels functionalized with CD-PDMA-RGD (**e**) and PNIPAM-RGD (**f**), respectively. ROI1(NIR illuminated) and ROI2 (non-illuminated). n = 55, 64, 57, 56 cells from left to right. ns p = 0.32835, 0.40963. Data was collected from at least 12 cell spheroids across three independent experiments. **g** Fluorescence imaging showing the expression of actin (grey), vinculin (green) and integrin αVβ3(red). Scale bars = 200 μm for 10× photo, 20 μm for magnified photos. **h** A significantly higher proportion of cells formed FAs after 4 cycles of illumination. Cells with focal adhesion were statistical results from 3 independent experiments, 3 spheroids each. The data in (**d**–**f**, **h**) is presented as mean values ± S.D. Data from non-illuminated and illuminated areas within each condition were compared using an unpaired one-tailed Student's t-test.
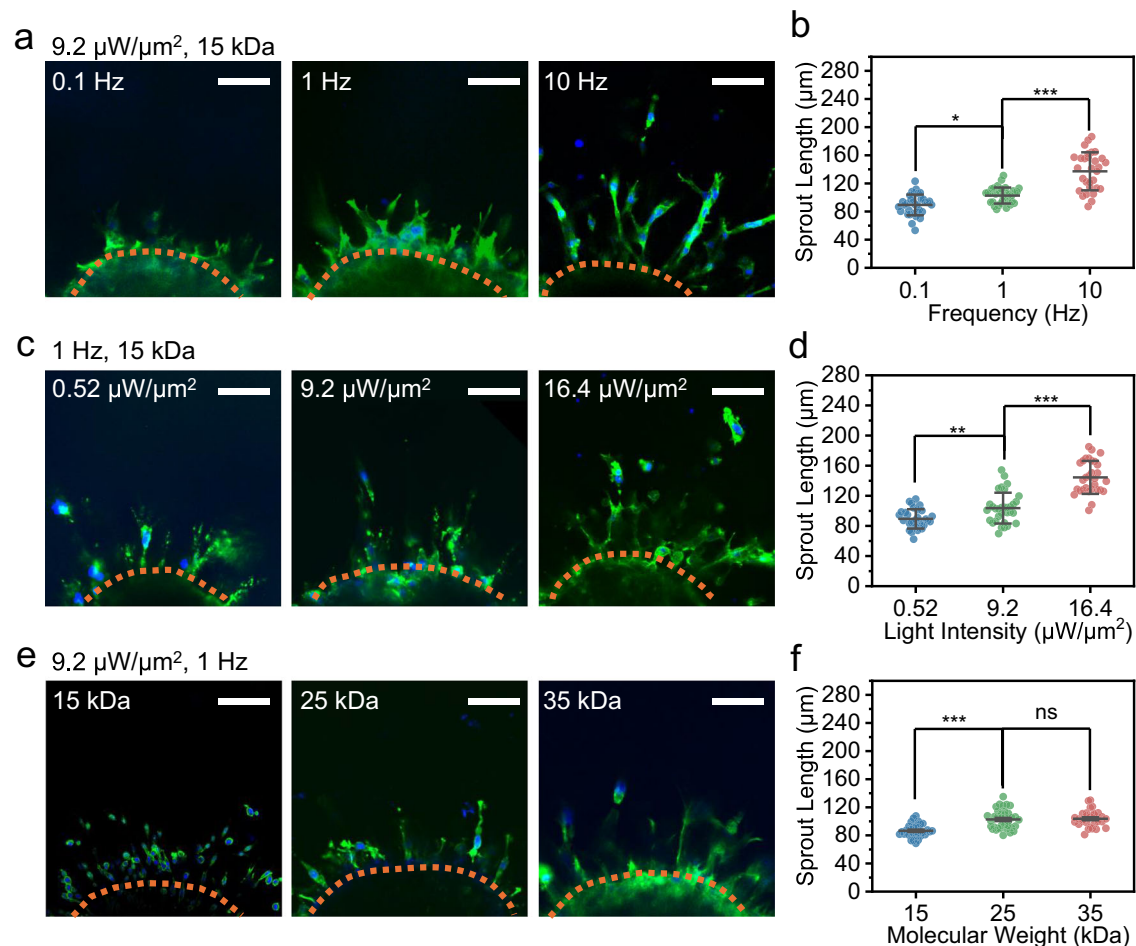

Fig. 4 | Force-induced cellular migration under various conditions.
a Fluorescent image of cell spheroids under different NIR power densities.
b Measurement of sprout length from cells under different pulsed frequencies (n = 33, 33, 30 cells). **c** Fluorescent image of spheroids under pulsed frequency stimulation. *P = 0.01272, ***P < 0.001 **d** Measurement of sprout length under different NIR power densities (n = 31, 32, 29 cells). **P = 0.00905, ***P < 0.001
e Fluorescent image of spheroids under varying actuator contour lengths.
f Measurement of sprout length under different actuator contour lengths (n = 31,

35, 30 cells). ***P < 0.001, ns P = 0.94032 Actin and nuclei are visualized as green and blue, respectively. Scale bars = 100 μm. Incubation temperature = 25 °C. Data were collected from at least eight cell spheroids in three independent experiments for each condition. Data from different conditions were compared using a one-way analysis of variance (ANOVA) followed by Tukey's post hoc test. Increasing illumination frequency, power density or molecular weight of the CD-PNIPAM-RGD actuator significantly enhanced cell migration, however, beyond a certain threshold, further increases in molecular weight did not yield additional improvement.

pronounced pulling effect (Fig. 4d). The contour length of the actuators, which directly influences the amplitude of force applied to receptors, could be finely adjusted through RAFT polymerizations. To illustrate this principle, we utilized three distinct actuators with contour lengths of 29 nm (15 kDa), 48 nm (25 kDa), and 74 nm (35 kDa) (Supplementary Fig. 7). According to our previous simulations[35], the pulling forces generated by these photothermal actuators for cellular experiments were anticipated to range between 150 and 400 pN. As anticipated, samples with longer actuators exhibited greater migration

displacements, suggesting that actuators of varying molecular weights can exert different levels of force on specific cellular receptors (Fig. 4e, f). This force estimation aligns with a modified freely-jointed chain (FJC) model reported by W. K. Zhang et al. based on their Atomic Force Microscopy (AFM) measurement[36]. This model demonstrates that the force exerted on PNIPAM chains scales linearly with their contour length, a finding consistent with our results, which indicate a force range of 140–330 pN. While tension sensors, such as DNA-based or vinculin FRET sensors, are widely utilized for measuring cellular

forces, their application is currently constrained by a detection limit of less than 100 pN[37]. Thus, the development of advanced optical tension sensors designed to precisely quantify forces across a broader range is urgent and currently under study. Loading rate can be derived from multiplying frequency and force applied to the cells. The loading rate, calculated by multiplying the frequency by the force applied to the cells, was scaled from 0.015 nN/s to 40 nN/s in our study. This range aligns with the loading rates reported in previous studies to effectively regulate cell behavior[17].

Intensive mechanical stimulation promotes cancer MAT depending on integrin subtypes

Under extended force stimulation, cells that expressed mesenchymal and collective cell migration were converted to the amoeboid mode. The amoeboid mode is characterized by less effective cell-extracellular matrix (ECM) interactions. This transition between the two modes is known as Mesenchymal-to-Amoeboid Transition (MAT)[3]. When we switched to 100 Hz for a 4-days force application period with a 35 kDa actuator, the cell initially exhibited mesenchymal migration mode for the first two days, followed by a pronounced MAT transition over the subsequent two days (Fig. 5a). Those amoeboid cells exhibiting rounded shapes and non-apoptotic bleb-like protrusions were found at the leading edge of the invasion front. To further confirm the phenotypic transition at the sub-cellular level, we employed immunofluorescence to identify markers of MAT (Fig. 5b). Our findings indicate that those cells with a round shape exhibit elevated expression of the transcription factor SNAI1 (Fig. 5c) and significantly reduced expression of E-cadherin (Fig. 5d), which is predominantly located around the nucleus. These observations strongly confirm that a MAT transition has occurred. With this transition, the cells became more deformable due to their lack of adhesiveness, allowing them to squeeze between matrix barriers and undergo a rapid gliding movement exceeding $20.8 \pm 4.0\,\mu m$/hour (See Supplementary Fig. 8d and Supplementary Movie 1).

To further confirm that the force application to receptors is the cause of MAT, we functionalized our hydrogels with an actuator containing another ligand CD-PNIPAM-RTD (see supplementary information for synthesis details) (Fig. 5e). RTD specifically targets αvβ6 integrin with high selectivity and binding affinity (Supplementary Table 1). Under the same force application conditions (35 kDa actuator and 100 Hz), cells exhibited mesenchymal collective migration in the early stage, but no MAT transition was observed at a later stage. The average migration speed was approximately 11.1 ± 4.1 µm/hour (See Supplementary Fig. 8d and Supplementary Movie 2). To elucidate the dynamics of integrin αvβ6, we conducted an ELISA assay on supernatants collected during illumination experiments, which revealed a significant upregulation of TGF-β1 expression in illuminated cells compared to the control group (Supplementary Fig. 9). This finding aligns with established literature demonstrating that αVβ6 activation facilitates TGF-β1 maturation[38]. While TGF-β1 ELISA serves as a useful proxy for assessing αvβ6 activation, we acknowledge that it represents an indirect measure of the whole spheroids' TGF-β1 secretion rather than a direct readout of integrin activity.

Next, we systematically investigate the extent of MAT transitions targeting different integrin subtypes with CD-PNIPAM-RGD and CD-PNIPAM-RTD under various conditions (Fig. 5f–h, Supplementary Fig. 10). Our findings indicate obvious MAT transitions occur with CD-PNIPAM-RGD, which are more pronounced under conditions of high-frequency and large-amplitude force application. Specifically, the incidence of MAT surged from 12 to 14% to 24.3% when frequency changed from 1 Hz to 100 Hz using a 35 kDa actuator (Fig. 5f). Similarly, within a power density range of 9.2–27.6 µW/µm², the MAT ratio escalated from 7% to 23%. For contour length, low MAT ratio was observed at 15 kDa, but it increased significantly at 25 kDa and 35 kDa

under 100 Hz (Fig. 5h). In contrast, minimum MAT transitions were observed in the case of CD-PNIPAM-RTD under all tested conditions. We also analyzed the maximum migration distance of amoeboid cells activated with CD-PNIPAM-RGD in each field of view under various stimulation conditions. A correlation was observed between the cell MAT ratio and the maximum migration length of amoeboid cells, with an increase in frequency, amplitude, and molecular weight corresponding to a longer maximum migration distance (Fig. 5i–k). The migration of mesenchymal cells activated by CD-PNIPAM-RTD exhibits a similar tendency to what was observed with CD-PNIPAM-RGD, as frequency, amplitude, and molecular weight increase, the cells' migration was enhanced.

Amoeboid cell migration is characterized by its independence from adhesions and can be triggered by disrupting cell-substrate adhesions, typically used in mesenchymal migration. We hypothesize that applying force at higher frequencies and amplitudes may disrupt the RGD-αvβ3 integrin adhesions, causing cells to reduce their reliance on sustained integrin-mediated adhesions. Instead, they explore and secure new attachment points through dynamic filopodia and lamellipodia, prompting a switch to an amoeboid migration strategy which is less dependent on adhesion. However, such force does not break RTD-αvβ6 adhesions, leading to mesenchymal migration behavior under the same force application condition.

Validated pathway impacts through molecular mechanics simulations

A molecular docking study was conducted to investigate the differential phenomenon observed after illumination with various ligands on the force-applying molecule. The RTD ligand utilized in this study is known for its strong combination affinity to integrin αvβ6 subtype[39] and shares the same active site sequence as the L-TGF-β3 peptide[40]. Docking calculations were performed using the structure derived from homology modeling of the peptide in the crystal structure of αvβ6[41]. Additionally, molecular docking was carried out using the XRD-derived crystal structure of the integrin αvβ3[42] in the complex with RGD. The top-ranked docking poses revealed that RTD can recognize these receptors by mimicking the canonical RGD interaction pattern (Fig. 6a). The results indicated that salt bridge, hydrogen bonds and Van der Waals forces significantly contributed to the ligand-receptor interaction. Specifically, for integrin αvβ3 and RGD, the ligand ASP[3] carboxylate group chelates the divalent cation at the metal-ion dependent adhesion site (MIDAS), while the ARG[1] guanidinium moiety of RTD establishes a side-on tight salt bridge with the conserved (αv)-D218 residue (Fig. 6a, Supplementary Fig. 11). For integrin αvβ6 and RTD, the ligand Leu[7] carboxylate group chelates the divalent cation at the metal-ion dependent adhesion site (MIDAS), forming an additional H-bond with the backbone of (β6)-A216. Meanwhile, the ARG[1] guanidinium moiety of RTD establishes a side-on tight salt bridge with the conserved (αv)-D218 residue and ARG[8] establishes a side-on tight salt bridge with the (β6)-A216 (Fig. 6b, Supplementary Fig. 12). Molecular Mechanics Generalized Born Surface Area (MMGBSA) docking energy calculation reveals that complex of integrin αvβ6 and RTD relatively higher affinity than integrin αvβ3 and RGD (Supplementary Table 2).

To further elucidate the unbinding dynamics of different ligand types and their interaction mechanisms with integrin αvβ3 and αvβ6 at the atomic level, we conducted steered molecular dynamics (SMD) simulations. After reaching equilibrium (Supplementary Fig. 13), external forces were applied to the Cα atom of the ligand's C-terminus to facilitate binding with the integrins (Fig. 6c). The pulling speed was set at $v = 0.06\,\text{Å·ps}^{-1}$, as established in previous studies[43]. The rupture force profiles along the dissociative trajectories are shown in Fig. 6d. It was observed that the rupture force required to detach the longer RTD ligand from the β6 binding site was 647 pN, which was significantly larger than the 400 pN required for the dissociation of the linear RGD
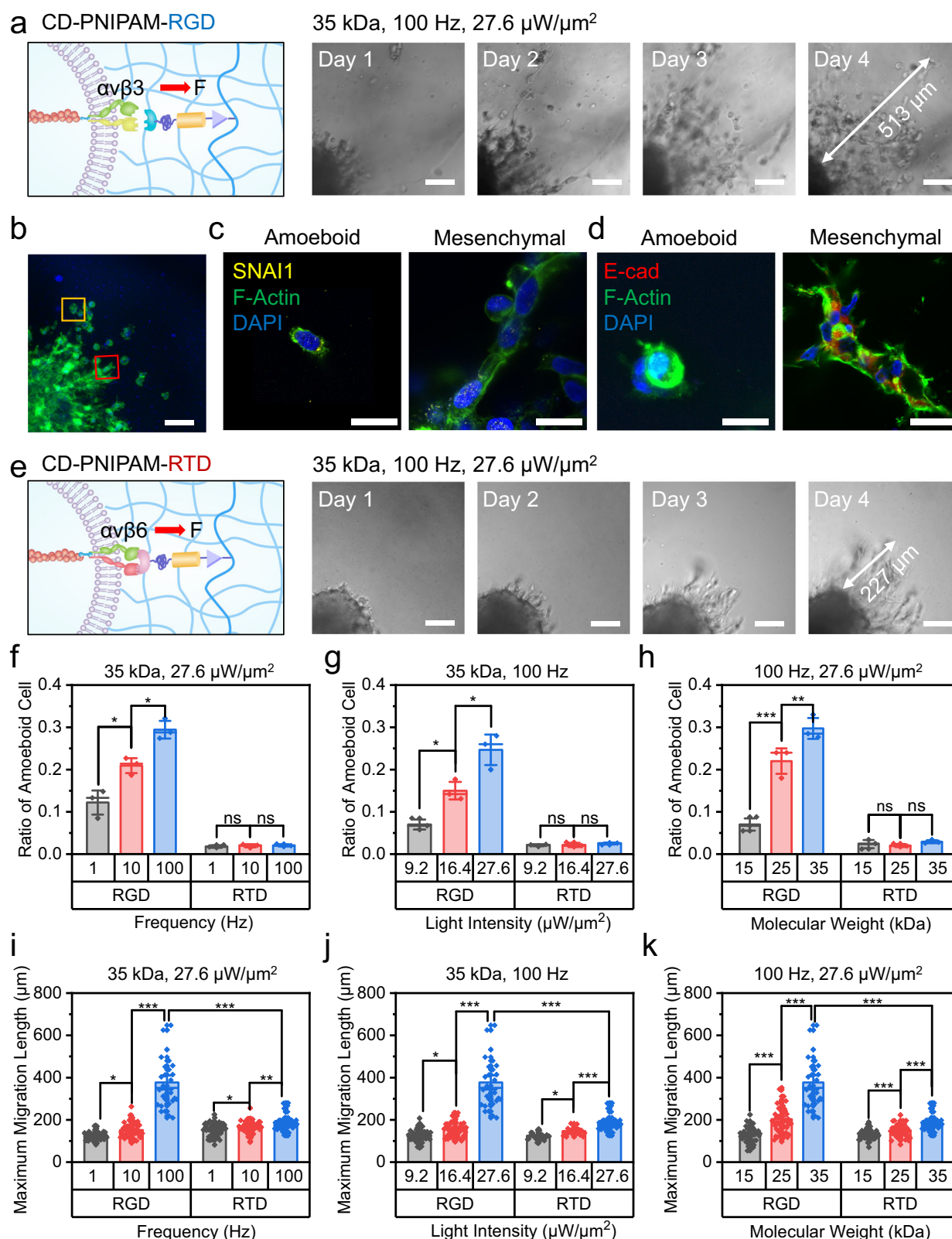
peptide from β3 (Fig. 6e). The differences in rupture force profiles indicate that the RGD ligand unbinds more easily than the RTD ligand. Given that our molecular tool applies forces ranging from 150 to 400 pN depending on the molecular weight[35], 35 kDa actuators are more capable of dissociating RGD from αvβ3 compared to 15 kDa and 25 kDa, thereby triggering a MAT that are less dependent on adhesions. This force, however, is insufficient to dissociate RTD from αvβ6,

only initiating mechanotransduction that leads to faster migration while maintaining the mesenchymal mode. Our simulation validates our experimental results and underscores the importance of material platforms capable of delivering precise forces to specific mechanosensors. Our platform allows for a more detailed and accurate investigation of the impact of mechanical forces on cancer cell migration mediated by various receptor subtypes.

Fig. 5 | Illustration of different cell migration patterns under intensive force application with CD-PNIPAM-RGD and CD-PNIPAM-RTD. a Schematic of integrin αvβ3 activated with CD-PNIPAM-RGD and time-lapse brightfield images showing cell migration over a 4-day period. Scale bar: 100 μm. **b** Fluorescent images at day 4 from **a**. Scale bar: 100 μm. **c** Representative images displaying enhanced SNAI1 expression in amoeboid cells compared with mesenchymal cells. Scale bar: 10 μm. **d** Representative images displaying enhanced E-cadherin expression in mesenchymal cells compared with amoeboid cells. The immunostaining images of actin are highlighted in green and the nuclei (DAPI, 4,6-diamidino-2-phenylindole) in blue, SNAI was presented in yellow and E-cadherin was presented in red. **e** Schematic of integrin αvβ6 activated with CD-PNIPAM-RTD and time-lapse brightfield photograph showing cell migration over a 4-day period. Scale bar: 100 μm. **f–h** Quantitative analysis of cell phenotype distributions from cells in hydrogels functionalized with CD-PNIPAM-RGD or CD-PNIPAM-RTD after 4 days of force application, used to evaluate the effects of (**f**) pulsed frequency, (**g**) NIR power densities, and (**h**) actuator molecular weight (Mw). **f–h** Each data point represents an independent spheroid (biological replicate, $n = 9$ spheroids/group, 3

experiments). For (**f**) $*P = 0.01565$, $*P = 0.01766$, ns $= 0.62788$, ns $= 0.75417$, (**g**) $*P = 0.03366$ $*P = 0.01495$, ns $P = 0.97658$, ns $P = 0.58146$ (**h**) $**P = 0.00126$, $*P = 0.02328$, ns $P = 0.84325$, ns $P = 0.34575$. **i–k** Quantitative analysis of cell maximum migration length after 4 days of force application, used to evaluate the effects of **i** pulsed frequency, **j** NIR power densities, and **k** actuator molecular weight (Mw). (**i-k**) The sample sizes for each condition are as follows: (**i**) $n = 54, 54, 30, 65, 65, 60$ cells (**j**) $n = 54, 65, 30, 24, 25, 60$ cells (**k**) $n = 53, 48, 30, 51, 50, 60$ cells from left to right taken from 9 spheroids respectively. For (**i**) $*P = 0.04095$, $***P < 0.001$, $*P = 0.04568$, $**P = 0.0928$, (**g**) $*P = 0.04611$ $***P < 0.001$, $*P = 0.04282$, $***P < 0.001$ (**h**) $***P < 0.001$, $***P < 0.001$, $**P = 0.0764$, $***P < 0.001$. The data in f-k are presented as mean values ± S.D. Data from different conditions were compared using a one-way analysis of variance (ANOVA) followed by Tukey's post hoc test. For CD-PNIPAM-RGD actuators, increased illumination frequency, power density, and actuator molecular weight enhanced both cell MAT and migration. In contrast, for CD-PNIPAM-RTD actuators, these increases improved cell migration but did not significantly affect the MAT ratio.

Discussion

In this study, we expanded upon our previous work by incorporating molecular actuators CD-PNIPAM-RGD into a Dextran-based hydrogel, creating an innovative platform capable of applying localized forces to specific cellular receptors within a 3D microenvironment. These actuators, which utilize a croconaine dye (CD) chromophore that converts near-infrared (NIR) light into heat, trigger thermal-responsive PNIPAM chains to shrink and exert tensile forces on targeted cell receptors. Using this advanced system, we examined how different mechanical force parameters—magnitude, frequency, and duration—impact the migration and invasion behaviors of ovarian cancer Hey cell spheroids. To further understand the role of specific integrin subtypes in these processes, we functionalized the actuators with two distinct subtype-specific ligands: RGD for αvβ3 and RTD for αvβ6 integrins. Our findings demonstrate that the application of mechanical force enhances collective cell invasion in the early stages of cell movement. Additionally, we observed a significant mesenchymal-to-amoeboid transition (MAT) during later stages, particularly when RGD-αvβ3 complexes were subjected to high-frequency and high-amplitude forces. Conversely, cells stimulated through RTD-αvβ6 complexes exhibited minimal MAT under similar conditions. Molecular mechanics simulations further validated these observations, highlighting the crucial role of specific force parameters and integrin interactions in modulating cell behavior. Notably, our approach offers distinct advantages over alternative methods: while optogenetic/optomechanical systems require genetic modification or invasive photoactivation, which disrupt native cell signaling and are chemically incompatible with 3D hydrogels, and electro-mechanical/magneto mechanical approaches often lack molecular-scale precision due to bulk force transduction (e.g., via magnetic beads or electric fields), our platform enables precise, non-invasive force application with greater molecular precision in 3D environments. This capability positions our system as a powerful tool for mechanotransduction research, providing valuable insights into the relationship between primary mechanical stimulation mediated by specific receptor subtypes and cellular behaviors. Consequently, this platform not only advances our fundamental understanding of cellular mechanics but also paves the way for the development of targeted therapeutic strategies and more sophisticated biomimetic materials.

Methods

Materials

N, N-dimethyl-formamide (DMF, 99.9%), triethylamine (TEA, 99%), acetone (99.7%), copper (II) sulfate (98%), edetate disodium dihydrate (99%), ethyl alcohol (75%), ethyl alcohol (95%), sodium ascorbate (99%), ether (99.5%), dodecanethiol (99%), carbon disulfide (CS_2, 99), 2-bromo-2-methylpropionic acid (99%) and chloroform-D (99.8%) are

purchased from Aladdin. 2-bromothiophene (98%), 2-dodecylsulfanylthiocarbonylsulfanyl-2-methyl-propionic acid 3-azidopropyl ester (98%) are ordered from Sigma–Aldrich. N-Isopropylacrylamide (NIPAM, 98%) was purified by recrystallization thrice from a mixture of acetone and hexane (1/4, v/v). 2,2-Azobis(2-methylpropionitrile) (AIBN, 98%) was recrystallized twice from 95% ethyl alcohol. N, N-Dimethylacrylamide (DMA, 98%) was passed through a small column of basic alumina for inhibitor removal prior to polymerization. All the water used was Milli-Q water. All the reagents and solvents were used as received unless otherwise stated.

Synthesis of DexMA

Dextran (Aladdin, Mw 70,000 Da) was modified with methacrylate groups, as previously described[32]. In brief, dextran (20 g) and 4-dimethylaminopyridine (2 g) were dissolved in 100 mL anhydrous dimethyl sulfoxide, and varying amounts of glycidyl methacrylate (GMA) were added under vigorous stirring. The mixture was heated to 45 °C and allowed to react for 24 hours (Supplementary Fig. 19). The solution was then cooled on ice and precipitated into 1 L ice-cold 2-propanol. The crude product was recovered by centrifugation, re-dissolved in Milli-Q water, and dialyzed against Milli-Q water for 7 days, with solvent exchanges twice daily. Finally, the solution was lyophilized to obtain the pure product, which was characterized by ^1H NMR spectroscopy in D_2O. The degree of functionalization was calculated as the ratio of the proton integral (6.174 and 5.713 ppm) to the anomeric proton of the glucopyranosyl ring (5.166 and 4.923 ppm). Since the signal of the anomeric proton of α-1,3 linkages (5.166 ppm) partially overlaps with other protons, a predetermined ratio of 4% α-1,3 linkage was assumed. The total anomeric proton integral was calculated solely based on the integral at 4.923 ppm. A methacrylate/dextran repeat unit ratio of 0.75 was determined.

Synthesis of the RAFT agent

5-(5-((2-((1-(3-((2-(((dodecylthio)carbonothioyl)thio)-2 methylpropanoyl)oxy)propyl)-1H-1,2,3-triazol-4-yl)methoxy)ethyl)(ethyl)amino) thiophen-2-yl)-2-(5-(ethyl(2-(prop-2-yn-1-yloxy)ethyl)amino)thiophen-2-yl)-3,4-dioxocyclopent-1-en-1-olate (CD-TTC) was synthesized using previously reported methods[29,35] (see Supplementary Fig. 20). ^1H NMR (400 MHz, $CDCl_3$) δ 8.82- 8.54 (m, 3H), 6.48 (s, 3H), 4.60 (s, 5H), 4.36 (s, 5H), 4.12 (s, 2H), 4.06 (s, 4H), 3.89-3.52 (m, 20H), 3.22 (t, J = 7.3 Hz, 5H), 2.42 (s, 1H), 2.20 (s, 5H), 1.71-1.53 (m, 19H), 1.35-1.14 (m, 55H), 0.83 (t, J = 6.6 Hz, 7H).

2-(Dodecylthiocarbonothioylthio)-2-methylpropionic acid (DDMAT) was prepared according to the procedure reported in previous literature[44] (see Supplementary Fig. 21). Dodecanethiol (5.0 mL, 20.9 mmol, 1.3 eq.) and K_3PO_4 (3.60 g, 16.9 mmol, 1.1 eq.) were combined in a 100 mL round-bottomed flask with 70 mL of acetone. After
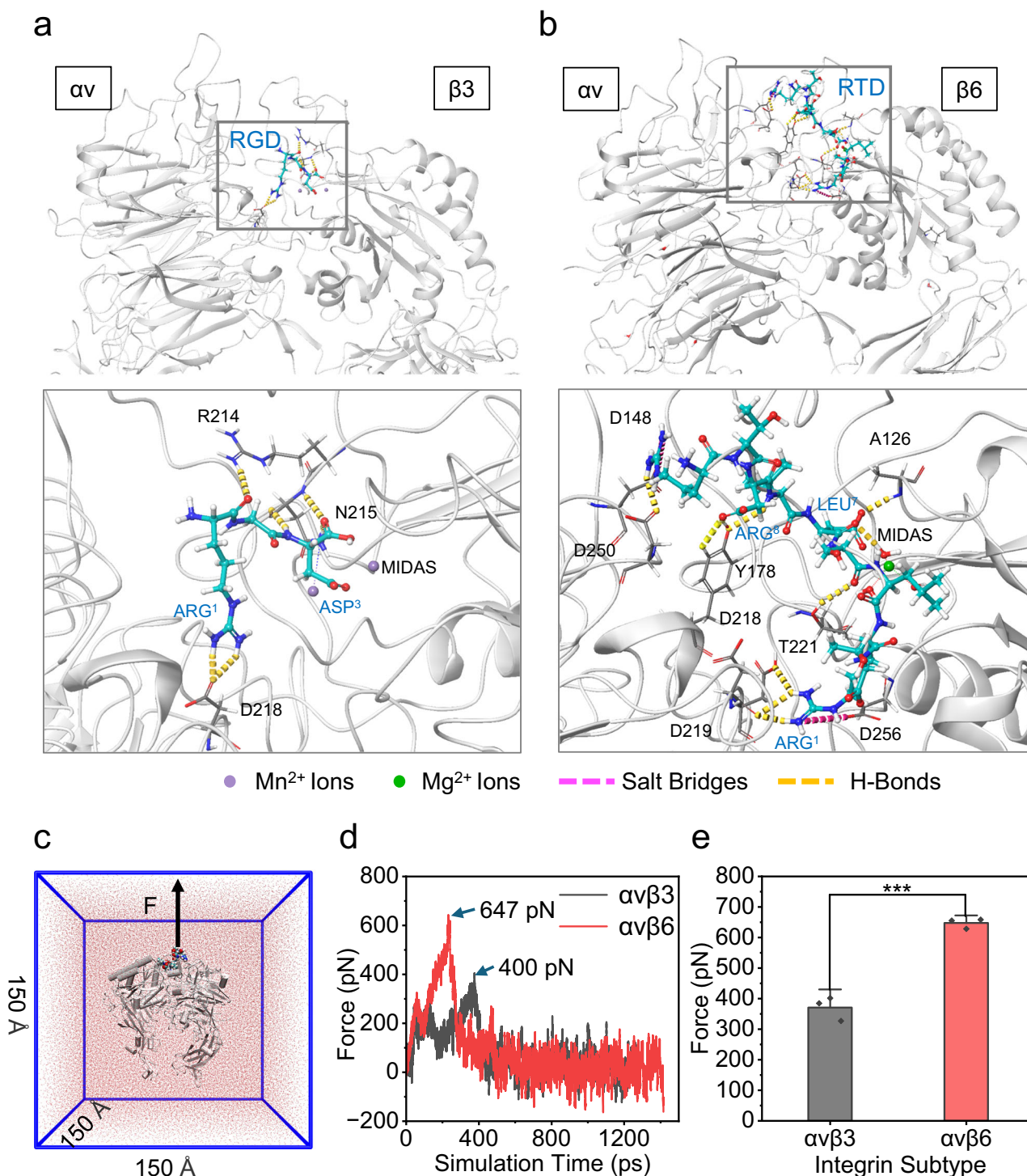
Fig. 6 | Computational analysis of integrin–ligand interactions and force-induced dissociation dynamics. a, b Interactions between the ligand motif and (**a**) αvβ3 integrin and (**b**) αvβ6 integrin (RGD/αvβ3 complex Protein Data Bank (PDB) ID: 1L5G, RTD/αvβ6 complex obtained from molecular docking). **c** The ligand bound to the integrin headpiece in a water box used for equilibration and steered molecular dynamics (SMD) simulations. **d** Force-induced dissociation trajectory of the ligand from integrin αvβ3 through steered molecular dynamics. The force profiles were obtained from five independent simulations, with the ligand being pulled away from integrin at a speed of $v = 0.06$ Å·ps^{-1} **e** Average peak force required for dissociation. For every group, the force calculated were from the same initial state of simulation but with different random seeds. The data in (**e**) is presented as mean values ± S.D. ***$P = 0.000179$.

stirring for 20 minutes, CS$_2$ (3.0 mL, 49.6 mmol, 3.1 eq.) was added dropwise to the previous mixture, during which the reaction solution turned yellow. 2-bromo-2-methylpropionic acid (2.64 g, 15.8 mmol, 1.0 eq.) was added to the stirring solution in one portion and continued to stir overnight at room temperature. 200 mL of 1 M HCl (ag) was added to the reaction mixture and then poured into a separatory funnel. The mixture was extracted with DCM (2 × 150 mL). The combined organic layers were dried over MgSO$_4$, and the solvent was removed under reduced pressure. The crude product was recrystallized from hexanes to afford DDMAT as yellow crystals (3.74 g, 65% recovery). ^{1}H NMR (400 MHz, CDCl$_3$) δ3.26 (t, 2H), 1.70 (s, 6H), 1.65 (m, 2H), 1.36 (m, 2H), 1.23 (m, 16H), 0.86 (t, 3H).

Preparation of polymer

In a typical synthesis, NIPAM or N,N-Dimethylacrylamide monomer (see Supplementary Table 3, 4 for detailed feed ratio), CD-TTC (4.86 mg, 0.005 mmol) and AIBN (1.64 mg, 0.01 mmol) were dissolved in 0.5 mL of DMF in a Schlenk tube. The mixture was degassed with 3 freeze-evacuate-thaw cycles, backfilled with nitrogen, and heated at 80 °C (Supplementary Figs. 22, 23). After 48 h, the Schlenk tube was quenched in ice to stop polymerization. The crude solution was reprecipitated into an excess solution of acetic ether three times. The resulting brown powder was dried overnight under vacuum at room temperature to obtain CD-PNIPAM-TTC or CD-PDMA-TTC. The powder was then stored at −20 °C.

For polymerization of PNIPAM, NIPAM (113.16 mg, 1 mmol), DDMAT (1.82 mg, 0.005 mmol) and AIBN (0.82 mg, 0.005 mmol) were dissolved in 0.5 mL of DMF in a Schlenk tube. The mixture was degassed with 3 freeze-evacuate-thaw cycles, backfilled with nitrogen, and heated at 80 °C (Supplementary Fig. 24). After 48 h, the Schlenk tube was quenched in ice to stop polymerization. The crude solution was reprecipitated into an excess solution of acetic ether three times. The obtained brown powder was then dried overnight under vacuum at room temperature s(see Supplementary Table 5 for detailed feed ratio).

CD-PNIPAM-TTC (75 mg, Mw 15 kDa, 5×10^{-6} mol) was dissolved in a 1 mL mixture of DMF: water = 3:1 (v/v). The solution was first reacted with hydrazine hydrate for 5 min to perform an ammonolysis reaction. Subsequently, 1 M hydrochloric acid was added to adjust the pH to 7, followed by the addition of 1.2 equivalents of 3-Maleimidopropionic acid-RGD (GL Biochem, category no. RD-3) for a thiol-ene reaction. After 30 minutes of reaction, the pH was adjusted to 9 using 1 M sodium hydroxide, and 5 equivalents of 2,2′-[1,2-ethanediylbis(oxy)] bis(ethanethiol) were added. Finally, the crude solution was reprecipitated into an excess of acetic ether three times.

HS-CD-PDMA-RGD and HS-CD-PNIPAM-RTD were prepared using a similar synthetic route, with the regent CD-PNIPAM-TTC replaced by CD-PDMA-TTC or Maleimidopropionic acid-RGD replaced by Maleimidopropionic acid-RTDLDSLRT (RTD) (Supplementary Figs. 25, 26).

For PNIPAM's end modification, PNIPAM powder (150 mg, Mw 15 kDa, 10^{-5} mol) was dissolved in 5 mL dry DMF and activated with EDC/NHS for 2 h. Subsequently, 1.5 equivalents of RGD were added. After the reaction, the crude solution was reprecipitated into an excess of acetic ether three times (Supplementary Fig. 27). The crude products (90.6 mg, 6×10^{-6} mol) were then redissolved in 1.2 mL of DMF:water = 3:1 (v/v) mixture and reacted with hydrazine hydrate for 5 min for ammonolysis. Dialysis was performed using a dialysis membrane with a molecular weight cut-off (MWCO) of 3500. The pH of the dialysis buffer was adjusted to 5 using acetic acid to prevent thiol oxidation. The dialysis buffer was changed twice daily.

Fabrication of hydrogel

Hydrogel without spheroid encapsulation was obtained using the following methods: DexMA (for synthesis of DexMA, see Supplementary Fig. 19) was dissolved in a buffer containing sodium bicarbonate (3.5% w/v) and HEPES (10 mM) to make a 20 wt% solution. CD-PNIPAM-ligands (for synthesis of CD-PNIPAM-ligand and other polymers, see Supplementary Figs. 20–27) were dissolved in PBS at a concentration of 5 mM. DexMA solution (20 wt%, 40 μL) was mixed with CD-PNIPAM-RGD (5 mM, 4 μL) and incubated at 37 °C for 30 min. After incubation, 36 μL of PBS was added to the mixture. Finally, 20 μL of NCD linker (150 mmol/L thiol groups) was added.

Swelling test

A hydrogel pre-mixture was placed in a PTFE mold for gelling. After gelling, the hydrogel was carefully removed from the mold and soaked in RPMI 1640 culture medium for 24 hours. A digital vernier caliper was used to measure the diameter with high precision.

Nuclear Magnetic Resonance (NMR) spectroscopy

^{1}H NMR spectra were recorded on an AVANCE NEO 400 (Bruker Biospin AG, Switzerland), 400 M Nuclear Magnetic Resonance (NMR) Spectrometer at a working frequency of 400 MHz for the ^{1}H nuclei using CDCl$_3$ as the solvent at room temperature.

Mass spectroscopy (MS)

Liquid chromatography and Orbitrap high-resolution mass spectrometry (LC-HRMS) was carried out on an Ultimate 3000-Q Exactive Focus (Thermo, USA) with an electrospray ionization (ESI) source. Agilent Mass Hunter Qualitative and Xcalibur software package was used to analyze the chromatogram and mass spectra.

Gel permeation chromatography (GPC)

GPC measurements were carried out on Viscotek TDAmax instrument (Malvern Panalytical, UK). The measurement was performed using a refractive index (RI) detector and THF was used as an eluent at a flow rate of 0.5 ml/min at 40 °C. A series of low polydispersity polystyrene standards were used for calibration.

Ultraviolet-visible (UV-vis) absorption spectroscopy. The optical absorption of polymer solutions and hydrogels was measured at 700–1000 nm using a UV-2600 UV-Vis spectrometer (Shimadzu, Japan) coupled with a temperature controller.

Scanning electron microscope (SEM). The concentration of the DexMA macromer was 8 wt% in the mixture, which also contained CD-PNIPAM-RGD with different molecular weights at a concentration of 1 mM. After freeze-drying, the samples were sputter-coated with gold and mounted on an SEM sample table using conductive adhesive. Imaging was conducted using an SEM (JSM-6010PLUS/LA, Japan) with a resolution of 1.0 μm at 5 keV.

Mechanical characterization for hydrogel

Oscillatory experiments were conducted using a rheometer (DHR, TA instruments) equipped with a 5 mm steel plate geometry and a Peltier heated plate, operated in a frequency-controlled, amplitude-controlled, or time-controlled mode. Strain sweeps with an oscillation frequency of 1 rad/s were performed over a strain range of 0.01–100% to determine the linear viscoelastic region. After identifying the linear viscoelastic region, the samples were subjected to a frequency sweep from 0.01 to 10 Hz. Mineral oil was applied to the hydrogel-air-instrument interface to prevent evaporative artifacts. Gelation was monitored by time sweep at 1 rad s^{-1}, 1% strain, and 37 °C.

Cell culture

Ovarian cancer Hey cell line was cultivated at 37 °C in 5% CO$_2$ in RPMI 1640 medium (Gibco), supplemented with 10% fetal bovine serum (Invitrogen) and 1% P/S (Invitrogen). Cells were used between passages P4 and P20.

Fabrication of hydrogel with spheroids

To fabricate hydrogels with spheroids, 10,000 cells were seeded in each well of a Corning® Costar® Ultra-Low attachment multiwell plate and incubated for 24 h to form spheroids. The cell medium was carefully removed, and the spheroids were washed once with PBS, collected into a 1.5 mL centrifuge tube, and briefly spun down at low speed (30 sec, 300 g) before removing the PBS. A DexMA solution (20 wt%, 40 μL) was mixed with cyclo(RGDfC) (5 mM, 16 μL) and CD-PNIPAM-RGD (5 mM, 4 μL), incubated at 37 °C for 30 min, and then RPMI 1640 medium (20 μL) was added. This mixture was used to resuspend the spheroids, followed by the addition of an NCD linker (150 mmol/L thiol groups, 20 μL). The resulting solution was placed into an Ibidi® 15 μ well angiogenesis slide for gelation. After incubation for 30 min at 37 °C, 50 μL cell

culture medium was added on top of the hydrogel to maintain hydration and support cell growth.

Live/Dead staining
Samples were stained with FDA/PI. Cell viability was evaluated at 24 h after gelation, 2 and 4 days after illumination. Viability was quantified across 9 spheroids per condition (3 independent experiments, 3 spheroids each) using Fiji/ImageJ. (Figure S3).

Immunofluorescence staining
Samples were fixed with 4% paraformaldehyde for 1 h at room temperature and permeabilized in PBS containing Triton X-100 (0.1 v/v%) for 15 min. To visualize the actin cytoskeleton and nuclei, samples were stained simultaneously with phalloidin-633 and DAPI for 30 min at room temperature. For immunostaining, gels were additionally blocked in 5% BSA for 1 h. Gels were then incubated in primary antibody diluted in 1% BSA overnight, followed by Alexa-conjugated goat anti-rabbit secondary antibodies (1:200 dilution, Abcam, category no. ab150077) for 1 h at room temperature. Subsequently, samples were washed twice with PBST (Phosphate-buffered saline with Tween-20) and three times with PBS. Then, Alexa Fluor 633 phalloidin (Zenbio) was used to label actin (1:200), and DAPI (BBI, E607303-0002) was used to label the nuclei (1:500).

Primary antibodies used were as follows: rabbit anti-E-cadherin (1:500, Abcam, category no. ab1416), rabbit p-Pax 1:100 (Tyr118) (Cell Signaling, category no. 69363), Snail (C15D3) Rabbit mAb (Cell Signaling, category no. 3879 T), mouse anti-human Integrin beta 3 Antibody (MCE, category no. HY-P80419) Mouse Anti-Integrin beta 1 antibody (Abcam, category no. ab24693) Mouse anti-Integrin alpha V beta 6 Antibody (Sigma-Aldrich, category no. ZRB1104).

Secondary antibodies used were as follows: Alexa-conjugated goat anti-rabbit or goat anti-mouse secondary antibodies (1:1000 dilution, Abcam, category no. ab150077, abbkine, category no. A22110). Fluorescent imaging was performed with a Leica SP8 laser scanning confocal microscope. For migration analysis, Z-stacks of spheroids situation greater than 150 μm from the glass bottom were acquired with a 10x objective. High-resolution images were similarly acquired with a 40x objective.

Quantification of cellular anisotropy
Anisotropy of actin filaments was quantified by performing analysis of confocal images (3 spheroids, 5 ROIs each group) using the ImageJ FibrilTool plugin[45].

Illumination
Laser actuation setup and exposure conditions: A custom-made setup was designed for the experiments, using an optical microscope equipped with an NIR laser, allowing simultaneous activation of the molecular actuators at 808 nm and real-time cell monitoring. The laser was directed directly from above the sample stage and focused on the hydrogel through a collimator. For more precise illumination, a focused light path consisting of double lenses was used to create a smaller light spot. A short-pass IR filter was included in the optical path to prevent the camera's CMOS sensor from exposure to converged IR light. The laser power reaching the gel was experimentally measured using a power meter, and the intensity was calculated based on the spot size observed through the microscope camera on the hydrogel. The laser footprint was maintained consistently across all experiments.

Different laser settings were applied, and a DDS signal generator/counter LE (OPTICS) was used to modulate the signals of laser light. Unless otherwise specified, typical illumination conditions for cell experiments were as follows: power density of 9.2 μW/μm², 10% duty cycle, and a laser spot diameter of 150 μm. Previous reports indicate that cells can respond to high-frequency mechanical loading induced by photothermal actuators[46], and that brief mechanical stimulation (e.g., 2 hours/day) is sufficient to trigger cellular mechanoresponses in 3D cultures[47]. Thus, samples in our experiments were subjected to a cyclic illumination regimen consisting of 1 h of illumination followed by 11 h of darkness, repeated every 12 h for at least 48 h.

Cell migration and morphology analysis
Maximum intensity projections of spheroid nuclei and F-actin channels were used as inputs to a custom Python code. Each channel was filtered with separate fluorescent intensity and area thresholds to remove background noise. A user-drawn ellipsoidal region of interest (ROI) covering the spheroid body was used to differentiate the spheroid body from outer cells. The user then confirmed each segmented F-actin structure as an outgrowth, after which the code determined whether an outgrowth was contiguous or noncontiguous with the spheroid body. A separate function segmented the overlapping nuclei to count the number of nuclei within the sprout. The two channels were then stacked to confirm the shape of the single cells. The aspect ratios of cells were compared, with individual cells having an aspect ratio of less than 2 being considered to exhibit amoeboid-like migration. During this process, a brightfield photo of the spheroid shape before illumination was used to quantify the distance of cell sprout migration to the nearest edge of the spheroid perimeter. As for motility analysis, cells' migration trajectories were extracted using TrackMate[48] and a set of statistical functions in Matlab provided by Wu, PH. et al.[49] was used to analyze motility, including speed, velocity autocorrelation function (ACF), mean square displacement (MSD), the probability density function of cell displacements (PDF-dRs), the probability density function of angular displacements (PDF-dθ), and the velocity profiles at different orientations (dR(θ)).

ELISA
HEY cell spheroids were encapsulated into DexMA hydrogel with CD-PNIPAM-RTD as mentioned above. Each hydrogel contained three cell spheroids. For each experiment, three hydrogels were subjected to NIR laser illumination as the experimental group, while another three hydrogels served as the control group without illumination. The light exposure cycle lasted for four days, and culture supernatants were collected daily to measure the concentration of TGF-β1. The concentration of TGF-β1 was determined using an ELISA kit according to the manufacturer's instructions (Shanghai ExCell Biology, Inc., Shanghai, China).

Molecular docking
Ligands used in our experiments were docked into the crystal structure of either the αvβ3 or αvβ6 complex with RGD or L-TGF-β3 peptide (PDB code: 1L5G and 4UM9, respectively[41,42]). Both the peptide and receptor structures were prepared using the Protein Preparation Wizard following established protocols[50]. Missing hydrogen atoms were added, and water molecules were removed from the receptor structures. The Mg^{2+}, Mn^{2+}, and Ca^{2+} divalent cations co-crystallized at the MIDAS site were retained with default settings. The Epik method[51,52] was used to predict the ionization and tautomeric states of the side chains. Before docking, the receptor was refined by optimizing its hydrogen-bonding network and minimizing hydrogen positions. A 25 Å × 25 Å × 25 Å virtual grid box centered on the ligand-binding site was generated using the Receptor Grid Generator tool in Glide 8.5[53]. Docking simulations were carried out with the default SP-peptide parameters in Glide, utilizing the OPLS-3e force field[54]. The top-ranked pose for each system was selected, with docking scores of −8.745 and −12.620 for the RGD ligand-αvβ3 pair and RTD ligand-αvβ6 pair of complexes, respectively.

Molecular dynamics
A simulated system of integrin αvβ6 binding with ligand RTDLDSLRT was set up for the MD simulations. The simulation for the system was

started from the structure of semi-flexible docking containing the complex of integrin αvβ6 with RTD ligand. Prior to the MD simulations, the complex was solvated in a 150 Å × 150 Å × 150 Å box using the TIP3P water model, Na^+ and Cl^- ions were added to neutralize the system and achieve a 0.15 M ionic concentration, resulting in a total of 325461 atoms. For the complex of integrin αvβ3 with RGD ligand, same procedures were conducted resulting in a total of 325,753 atoms. Due to the absence of Mn^{2+} force field parameters, a universal method in which Mn^{2+} was replaced by Mg^{2+}, the metal ion-binding sites in integrin $\alpha_v\beta_6$ were occupied by Mg^{2+} ions in our simulations.

All MD simulations were performed using the program GROMACS 2020.6[55], employing periodic boundary conditions and the Amber14sb force field[56]. The particle-mesh Ewald method was used for electrostatic calculations, while van der Waals interactions were evaluated using a smooth cutoff of 12 Å. Visualization, molecular graphics, and analyses of simulations, including root mean square deviation (RMSD), the distance between two atoms or the centers of mass of the helix, and solvent accessible surface area (SASA) with a 1.4 Å radius probe, were performed using Tool Command Language (Tcl) module within the VMD program[57]. A hydrogen bond was defined when the donor–acceptor distance was shorter than 0.35 nm, and the donor–hydrogen–acceptor angle was less than 30°. Occupancy was evaluated by the proportion of the bond survival time over the simulation time.

Each system was first subjected to energy minimization for two consecutive 50,000 conjugate gradient steps: first with backbone atoms fixed and second with all atoms free. The energy-minimized structures were gradually heated from 0 to 310 K and subsequently equilibrated for 10 ns under constant pressure and temperature conditions. The temperature was maintained at 310 K using Langevin dynamics, and the pressure was maintained at 1 atm using the Langevin piston method.

Constant velocity-steered molecular dynamics (SMD) simulations were performed to accelerate integrin unbinding, starting from snapshots sampled after 10 ns equilibration period. We used a time step of 2 fs, a uniform dielectric constant of 1.0, a 12 Å cut-off for non-bonded interactions, and a scaling factor of 1.0 for 1–4 interactions. During the SMD simulations, the ligand was pulled away from the binding shallow crevice located between the α and β subunits of the integrin headpiece. The C or N termini of the βA and β-propeller subunits were fixed as original points. The pulling potential moved with a constant velocity v, and the C-terminal Cα atom of ligand was steered as the SMD atom. In constant-velocity simulations, the time dependence of the external force is $F = k(vt - \Delta x)$, where Δx is the displacement along the pulling direction at time $t = 0$, v is the pulling velocity, and k is the spring constant. The rupture force presents the maximum of the force spectrum. Here, we set the pulling speed 0.06 Å·ps^{-1} and the spring constant as $k = 5$ kcal·mol^{-1}·Å^{-2}. The SMD simulation was performed in an NVE ensemble at 310 K and lasted for at least 400,000 steps.

Statistics and reproducibility

Statistical analyses were performed using Origin software. The data is expressed as mean ± standard deviation unless otherwise specified. Sample sizes are provided in figure captions, but typically, experiments were conducted with a minimum of $n = 3$ for each condition. Error bars represent the standard deviation. Images in this paper are taken from results obtained from 3 independent biological replicates, with similar results observed across all replicates.

For comparisons between two groups, an independent Student's t-test was used to determine whether there was a significant difference between their means. For comparisons among three or more groups, a one-way analysis of variance (ANOVA) followed by Tukey's post hoc test was conducted to identify significant differences among group means. Statistically significant differences were defined as at $p < 0.05$, 0.01, and 0.001 by *, **, and *** respectively.

Reporting summary

Further information on research design is available in the Nature Portfolio Reporting Summary linked to this article.

Data availability

The data supporting the findings of this study are available within the Article and its Supplementary Information. Source data are provided with this paper.

Code availability

All the code used to reproduce the analysis reported in this study have been deposited in Zenodo (https://doi.org/10.5281/zenodo.15356266).

References

1. Valet, M., Siggia, E. D. & Brivanlou, A. H. Mechanical regulation of early vertebrate embryogenesis. *Nat. Rev. Mol. Cell Biol.* **23**, 169–184 (2022).
2. Zhou, D. W. et al. Force-FAK signaling coupling at individual focal adhesions coordinates mechanosensing and microtissue repair. *Nat. Commun.* **12**, 2359 (2021).
3. Shieh, A. C. Biomechanical Forces Shape the Tumor Microenvironment. *Ann. Biomed. Eng.* **39**, 1379–1389 (2011).
4. Bakir, B., Chiarella, A. M., Pitarresi, J. R. & Rustgi, A. K. EMT, MET, Plasticity, and Tumor Metastasis. *Trends Cell Biol.* **30**, 764–776 (2020).
5. Saraswathibhatla, A., Indana, D. & Chaudhuri, O. Cell-extracellular matrix mechanotransduction in 3D. *Nat. Rev. Mol. Cell Biol.* **24**, 495–516 (2023).
6. Zanotelli, M. R., Zhang, J. & Reinhart-King, C. A. Mechanoresponsive metabolism in cancer cell migration and metastasis. *Cell Metab.* **33**, 1307–1321 (2021).
7. Pang, X. C. et al. Targeting integrin pathways: mechanisms and advances in therapy. *Signal Transduct. Target. Ther.* **8**, 1 (2023).
8. Chopra, A. et al. Augmentation of integrin-mediated mechanotransduction by hyaluronic acid. *Biomaterials* **35**, 71–82 (2014).
9. Panzetta, V., Fusco, S. & Netti, P. A. Cell mechanosensing is regulated by substrate strain energy rather than stiffness. *Proc. Natl Acad. Sci. Usa.* **116**, 22004–22013 (2019).
10. Yi, B. C., Xu, Q. & Liu, W. An overview of substrate stiffness guided cellular response and its applications in tissue regeneration. *Bioact. Mater.* **15**, 82–102 (2022).
11. Onal, S., Alkaisi, M. M. & Nock, V. Microdevice-based mechanical compression on living cells. *Iscience* **25**, 105518 (2022).
12. Das, K. K., Basu, B., Maiti, P. & Dubey, A. K. Interplay of piezoelectricity and electrical stimulation in tissue engineering and regenerative medicine. *Appl. Mater. Today* **39**, 102332 (2024).
13. Jeong, S. et al. Hydrogel Magnetomechanical Actuator Nanoparticles for Wireless Remote Control of Mechanosignaling. *Nano Lett.* **23**, 5227–5235 (2023).
14. Holuigue, H. et al. Native extracellular matrix probes to target patient- and tissue-specific cell–microenvironment interactions by force spectroscopy. *Nanoscale* **15**, 15382–15395 (2023).
15. Kadem, L. F. et al. High-Frequency Mechanostimulation of Cell Adhesion. *Angew. Chem. Int. Ed.* **56**, 225–229 (2017).
16. Sun, J. et al. Slow walk" mimetic tensile loading maintains human meniscus tissue resident progenitor cells homeostasis in photocrosslinked gelatin hydrogel. *Bioact. Mater.* **25**, 256–272 (2023).
17. Andreu, I. et al. The force loading rate drives cell mechanosensing through both reinforcement and cytoskeletal softening. *Nat. Commun.* **12**, 4229 (2021).
18. Jain, S. et al. The role of single-cell mechanical behaviour and polarity in driving collective cell migration. *Nat. Phys.* **16**, 802 (2020).
19. Riveline, D. et al. Focal contacts as mechanosensors: Externally applied local mechanical force induces growth of focal contacts by

an mDia1-dependent and ROCK-independent mechanism. *J. Cell Biol.* **153**, 1175–1185 (2001).

20. Piotrowski-Daspit, A. S., Tien, J. & Nelson, C. M. Interstitial fluid pressure regulates collective invasion in engineered human breast tumors via Snail, vimentin, and E-cadherin. *Integr. Biol.* **8**, 319–331 (2016).

21. Kanchanawong, P. & Calderwood, D. A. Organization, dynamics and mechanoregulation of integrin-mediated cell-ECM adhesions. *Nat. Rev. Mol. Cell Biol.* **24**, 142–161 (2023).

22. Koivisto, L., Bi, J. R., Häkkinen, L. & Larjava, H. Integrin αvβ6: Structure, function and role in health and disease. *Int. J. Biochem. Cell Biol.* **99**, 186–196 (2018).

23. Dhaliwal, D. & Shepherd, T. G. Molecular and cellular mechanisms controlling integrin-mediated cell adhesion and tumor progression in ovarian cancer metastasis: a review. *Clin. Exp. Metastasis* **39**, 291–301 (2022).

24. Dong, X. C. et al. Force interacts with macromolecular structure in activation of TGF-β. *Nature* **542**, 55 (2017).

25. Wang, X. F. & Ha, T. Defining Single Molecular Forces Required to Activate Integrin and Notch Signaling. *Science* **340**, 991–994 (2013).

26. Zheng, Y. J. et al. Optoregulated force application to cellular receptors using molecular motors. *Nat. Commun.* **12**, 3580 (2021).

27. Ramey-Ward, A. N. et al. Optomechanically Actuated Hydrogel Platform for Cell Stimulation with Spatial and Temporal Resolution. *ACS Biomater. Sci. Eng.* **9**, 5361–5375 (2023).

28. Yamada, K. M. & Sixt, M. Mechanisms of 3D cell migration. *Nat. Rev. Mol. Cell Biol.* **20**, 738–752 (2019).

29. Spence, G. T., Hartland, G. V. & Smith, B. D. Activated photothermal heating using croconaine dyes. *Chem. Sci.* **4**, 4240–4244 (2013).

30. Worch, J. C., Stubbs, C. J., Price, M. J. & Dove, A. P. Click Nucleophilic Conjugate Additions to Activated Alkynes: Exploring Thiol-yne, Amino-yne, and Hydroxyl-yne Reactions from (Bio)Organic to Polymer Chemistry. *Chem. Rev.* **121**, 6744–6776 (2021).

31. Zhou, N. et al. Effect of RGD content in poly(ethylene glycol)-crosslinked poly(methyl vinyl ether-alt-maleic acid) hydrogels on the expansion of ovarian cancer stem-like cells. *Mater. Sci. Eng. C. Mater. Biol. Appl.* **118**, 111477 (2021).

32. Trappmann, B. et al. Matrix degradability controls multicellularity of 3D cell migration. *Nat. Commun.* **8**, 371 (2017).

33. Rodríguez-Fernández, J., Fedoruk, M., Hrelescu, C., Lutich, A. A. & Feldmann, J. Triggering the volume phase transition of core-shell Au nanorod-microgel nanocomposites with light. *Nanotechnology* **22**, 240758 (2011).

34. Lou, J. Z., Stowers, R., Nam, S. M., Xia, Y. & Chaudhuri, O. Stress relaxing hyaluronic acid-collagen hydrogels promote cell spreading, fiber remodeling, and focal adhesion formation in 3D cell culture. *Biomaterials* **154**, 213–222 (2018).

35. Cheng, N. et al. Hydrogel platform capable of molecularly resolved pulling on cells for mechanotransduction. *Mater. Today Bio* **17**, 100476 (2022).

36. Zhang, W. K., Zou, S., Wang, C. & Zhang, X. Single polymer chain elongation of poly(-isopropylacrylamide) and poly(acrylamide) by atomic force microscopy. *J. Phys. Chem. B* **104**, 10258–10264 (2000).

37. Liu, X. et al. A multiplexed tension sensor reveals the distinct levels of integrin-mediated forces in adherent cells. *Mater. Adv.* **5**, 9220–9230 (2024).

38. Dhawan, U. et al. Mechanostimulation-induced integrin alpha(v) beta 6 and latency associated peptide coupling activates TGF-beta and regulates cancer metastasis and stemness. *Nano Today* **50**, 101882 (2023).

39. Tomassi, S. et al. Halting the Spread of Herpes Simplex Virus-1: The Discovery of an Effective Dual αvβ6/αvβ8 Integrin Ligand. *J. Med. Chem.* **64**, 6972–6984 (2021).

40. Kraft, S. et al. Definition of an unexpected ligand recognition motif for αvβ6 integrin. *J. Biol. Chem.* **274**, 1979–1985 (1999).

41. Dong, X. C., Hudson, N. E., Lu, C. F. & Springer, T. A. Structural determinants of integrin β-subunit specificity for latent TGF-β. *Nat. Struct. Mol. Biol.* **21**, 1091–1096 (2014).

42. Xiong, J.-P. et al. Crystal Structure of the Extracellular Segment of Integrin αVβ3 in Complex with an Arg-Gly-Asp Ligand. *Science* **296**, 151–155 (2002).

43. Montes, A. R. et al. Integrin mechanosensing relies on a pivot-clip mechanism to reinforce cell adhesion. *Biophys. J.* **123**, 2443–2454 (2024).

44. Chapman, R., Gormley, A. J., Herpoldt, K. L. & Stevens, M. M. Highly Controlled Open Vessel RAFT Polymerizations by Enzyme Degassing. *Macromolecules* **47**, 8541–8547 (2014).

45. Boudaoud, A. et al. FibrilTool, an ImageJ plug-in to quantify fibrillar structures in raw microscopy images. *Nat. Protoc.* **9**, 457–463 (2014).

46. Liu, Z. et al. Nanoscale optomechanical actuators for controlling mechanotransduction in living cells. *Nat. Methods* **13**, 143 (2016).

47. Sittichockechaiwut, A., Scutt, A. M., Ryan, A. J., Bonewald, L. F. & Reilly, G. C. Use of rapidly mineralising osteoblasts and short periods of mechanical loading to accelerate matrix maturation in 3D scaffolds. *Bone* **44**, 822–829 (2009).

48. Tinevez, J. Y. et al. TrackMate: An open and extensible platform for single-particle tracking. *Methods* **115**, 80–90 (2017).

49. Wu, P. H., Giri, A. & Wirtz, D. Statistical analysis of cell migration in 3D using the anisotropic persistent random walk model. *Nat. Protoc.* **10**, 517–527 (2015).

50. Sastry, G. M., Adzhigirey, M., Day, T., Annabhimoju, R. & Sherman, W. Protein and ligand preparation: parameters, protocols, and influence on virtual screening enrichments. *J. Comput. Aided Mol. Des.* **27**, 221–234 (2013).

51. Shelley, J. C. et al. Epik: a software program for pKaprediction and protonation state generation for drug-like molecules. *J. Comput. Aided Mol. Des.* **21**, 681–691 (2007).

52. Greenwood, J. R., Calkins, D., Sullivan, A. P. & Shelley, J. C. Towards the comprehensive, rapid, and accurate prediction of the favorable tautomeric states of drug-like molecules in aqueous solution. *J. Comput. Aided Mol. Des.* **24**, 591–604 (2010).

53. Friesner, R. A. et al. Glide: A new approach for rapid, accurate docking and scoring. 1. Method and assessment of docking accuracy. *J. Med. Chem.* **47**, 1739–1749 (2004).

54. Harder, E. et al. OPLS3: A Force Field Providing Broad Coverage of Drug-like Small Molecules and Proteins. *J. Chem. Theory Comput.* **12**, 281–296 (2016).

55. Abraham, M. J. et al. GROMACS: High performance molecular simulations through multi-level parallelism from laptops to supercomputers. *SoftwareX* **1–2**, 19–25 (2015).

56. Maier, J. A. et al. ff14SB: Improving the Accuracy of Protein Side Chain and Backbone Parameters from ff99SB. *J. Chem. Theory Comput.* **11**, 3696–3713 (2015).

57. Humphrey, W., Dalke, A. & Schulten, K. VMD: Visual molecular dynamics. *J. Mol. Graph.* **14**, 33–38 (1996).

Acknowledgements

Author contributions

Competing interests

Additional information